LC-DET-2007-006

A Luminosity Detector for the International Linear Collider

H. Abramowicz, R. Ingbir, S. Kananov, A. Levy

School of Physics and Astronomy, The Raymond and Beverly Sackler Faculty of Exact Sciences, Tel Aviv University, Tel Aviv Israel.

Abstract

This note summarizes the Monte Carlo studies of a tungsten-silicon sandwich calorimeter intended for precision measurement of luminosity at the future International Linear Collider. The studies, based on a pad readout, were conducted for single electrons as well as for Bhabha scattering, with radiative effects and beam spread, assuming a zero beam crossing angle. A possible design is presented for which the angular resolution would be sufficient to achieve a 10^{-4} relative precision on luminosity measurement.

1   Luminosity Measurement

In e^+e^- collider experiments, luminosity is determined by counting the number of small angle Bhabha scattering events and comparing it to the expected cross section, σ_B. The latter is well controlled theoretically, provided the beam spectrum is known, and efforts are being pursued to reduce the relative uncertainty down to less than 2.5×10^{-4} [1, 2], where the main contribution comes from higher order electroweak radiative effects.

At the future International Linear Collider (ILC), the colliding electron and positron bunches disrupt one another and induce radiation (beamstrahlung) which leads to significant energy loss and beam energy spread. In addition there might be an inherent energy spread of the collider. The beamstrahlung and the collider energy spread depend on the parameters of the collisions. Therefore at the ILC, the differential luminosity spectrum has to be measured on top of the integrated luminosity. In general, the collision parameters, such as the size of the collision region and bunch current, that lead to the highest luminosity, also lead to the largest smearing of the luminosity spectrum. In addition, the energy measurements can be tempered by the presence of beam related backgrounds, such as synchrotron radiation and thermal photons of the residual gas, backscattered off the electron beam.

The required accuracy of the luminosity measurement is derived from the physics program. The GigaZ program focuses on the measurement of fundamental parameters from the Z line-shape. In order to exploit the physics potential of GigaZ, the uncertainty on the luminosity must be as small as 2×10^{-4}[3]. Luminosity precision of better than 10^{-3} is necessary to study processes like $e^+e^- \to W^+W^-$ and $e^+e^- \to f^+f^-$ (where f denotes fermions) at high energies. The cross section for $e^+e^- \to W^+W^-$ is strongly forward peaked, largely dominated by t-channel neutrino exchange. A precise luminosity measurement is needed to probe anomalous $e\nu W$ couplings. The process $e^+e^- \to f^+f^-$ is sensitive to new physics at very high energy scales via interference with the Standard Model amplitude. To detect deviation from the Standard Model, precise cross section measurements are necessary.

The Bhabha process itself offers the possibility to determine the running of the electromagnetic coupling α as a function of the four-momentum transfer squared, q^2. The knowledge of $\alpha(q^2)$ is important because its current uncertainty limits the accuracy with which predictions for the electroweak quantities, such as the Higgs mass, can be made within the Standard Model. At GigaZ, the running of α can be probed for $q^2 > (1.2\,\text{GeV})^2$. In this q^2 region no precise cross section measurements of the process $e^+e^- \to$ hadrons exist [4].

Precision measurements of the leptonic and hadronic production cross sections in e^+e^- interactions are a significant part of all physics programs [5]. The precision with which such cross-sections can be measured is limited by the experimental error on the luminosity of the colliding beams. The best luminosity measurement was performed at LEP [6], based on small angle Bhabha scattering cross section measured in the OPAL silicon-tungsten luminometer. The achieved relative systematic precision on luminosity measurement was 3.4×10^{-4}, significantly below the relative theoretical uncertainty of 5.4×10^{-4} currently assigned to the QED calculation of the Bhabha scattering cross section [7]. With this level of accuracy at the ILC, the top quark mass could be determined with a precision of a few

tens of MeV [8] and the W boson mass could be measured to around 6 MeV [9]. Achieving this level of precision is one of the tasks facing the ILC community.

To achieve a precise determination of the Bhabha scattering rates, a good position and energy resolution of the luminometer are required. The position resolution is needed for the precise determination of the acceptance of the calorimeter; the energy resolution is needed to distinguish true Bhabha events from the off-momentum beam particles which contribute to the background.

2   The ILC Design

The linear collider will consist of two linear accelerators, for electrons and for positrons, bringing beams into either a head-on collision or a collision with a small crossing angle (up to 20 mrad) at the location of a large particle detector. To achieve the necessary collision energy, the overall complex will need to be more than 30 km long.

The challenges in the project are exemplified by the transverse beam sizes at collision (a few nanometers), by the requirement of very high electric field gradients to achieve large energies, and by the stringent control of the beams needed during the acceleration process.

The baseline center-of-mass energy will be 500 GeV, with the capability to lower the energy to about 90 GeV for some measurements and calibrations (GigaZ project [9]). An increase of the center-of-mass energy to 1 TeV will be possible. Several physics studies demand that the energy be adjustable so as to scan across particle production thresholds. To meet the physics goals, the machine luminosity at 500 GeV should be higher than 10^{34} cm^{-2} s^{-1}. The ability to distinguish many interesting processes from each other, and from backgrounds due to known reactions, is enhanced by providing longitudinal polarized electrons and positrons. The baseline electron beam polarization will be 80% [9].

2.1   Crossing angle

A big crossing angle in the interaction region would complicate the luminosity measurement. The beam particles and backscattered particles will have a bigger transverse momentum in the region of the magnetic field and the total background will increase. One of the challenges of this study will be to deal with the inhomogeneity and asymmetry in the ϕ angle of this background. A study of how the precision of the luminosity measurement be influenced by different crossing angles can be found elsewhere [10].

3   Bhabha Scattering

Elastic Bhabha scattering (see Fig 1) is the process

$$e^+ e^- \to e^+ e^- \ . \tag{1}$$

Pure elastic Bhabha scattering never occurs, as the process is always accompanied by the emission of electromagnetic radiation. The radiated photons are mostly emitted along the direction of the parent particles and therefore the intial state radiation remains undetected

in the beam pipe, while the final state radiation will be absorbed into the electromagnetic shower of the final state lepton.

Both γ and Z^0 exchange, in the s and the t channel, contribute to the differential Bhabha cross section (see [11]) as shown in Fig. 1. However, for small scattering angles, such as
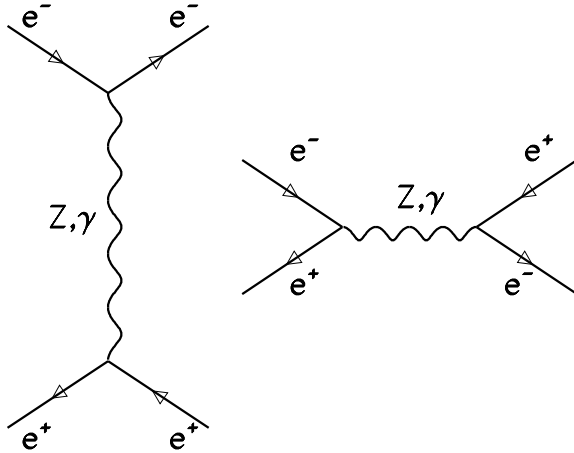

Figure 1: Feynman diagrams contributing to Bhabha scattering.

$\theta \leq 10°$, the Bhabha scattering is dominated ($\geq 99\%$ of the cross section) by the t channel exchange of a photon and the cross section can be expressed by

$$\frac{d\sigma}{d\Omega} = \frac{\alpha^2}{2s} \left[\frac{1 + \cos^4(\theta/2)}{\sin^4(\theta/2)} - 2\frac{\cos^4(\theta/2)}{\sin^2(\theta/2)} + \frac{1 + \cos^2\theta}{2} \right] , \qquad (2)$$

where the first and the last terms correspond to γ exchange in the t and s-channels respectively, while the second term reflects the $s - t$ channel interference. The angle θ is the polar angle of the scattered electron (positron) with respect to the beam, α is the fine structure constant and s is the center-of-mass energy squared. At small values of θ the angular spectrum has a simple approximate form $d\sigma/d\theta \propto 1/\theta^3$.

The total Born cross section for Bhabha scattering integrated over $27 \leq \theta \leq 80$ mrad is about 6 nb at $\sqrt{s}$=500 GeV. For the expected luminosity of $\mathcal{L} = 3.4 \cdot 10^{34}$ cm^{-2} s^{-1} the resulting event rate, R_{ev}, is about 200 Hz.

4 Beamstrahlung

Since the trajectories of the moving particles in the bunches are bent due to the pinch effect, they emit radiation called beamstrahlung. Usually beamstrahlung is characterized by a dimensionless parameter called the global beamstrahlung parameter Υ. The Υ parameter controls the overall radiation intensity and depends only on averaged global beam parameters [12, 13] , The average value of Υ for the proposed collider is ~ 0.05. This results in a mean number of emitted photons due to beamstrahlung of $n_\gamma \simeq 1.6$ per electron.

3

The average radiative energy loss due to beamstrahlung, δ_E, is $\sim 4\%$. This means that by decreasing σ_y one can increase the luminosity while the energy loss remains unchanged. The average photon energy is $< \omega > \approx 2.3\% \ E_{\text{beam}}$.

5   Forward Region Layout

Three detectors are intended to cover the very forward region of the future ILC detector. These are the BeamCal, for fast luminosity feed-back and for detector hermeticity, the GamCal for luminosity monitoring and the LumiCal for luminosity measurement.

The maximal distance between the forward calorimeters BeamCal and LumiCal and the interaction region is mainly determined by the focal length $L^\star$ of the final focus system. In the present study a value of $L^\star = 4.15$ was used [14]. The schematic view of the layout is shown in Fig. 2.

6   Basic design of LumiCal

The LumiCal covers polar angles θ from 26 to 91 mrad with respect to the beam line. The LumiCal is composed of segmented silicon sensors layers interspersed between tungsten disks. Each layer is composed of a silicon sensor plane of 500 μm thickness and a tungsten-silicon mixture of 0.34 cm of tungsten and 0.31 cm silicon sensors and electronics. The composition reflects the presence of electronic boards, which will be inserted on both sides of each tungsten plate. The resulting module thickness is 0.65 cm and corresponds to one radiation length [16].

The LumiCal is expected to have sufficient depth and a fine segmentation. The detector is subdivided radially into 15 cylinders, azimuthally into 24 sectors and longitudinally into 30 layers. The transverse granularity is shown in Fig. 3. The cell transverse size is one Moliére radius. The total number of cells (electronic channels) is 10,800.

Two identical calorimeters, one on the electron side and the second for the positron side are positioned at a distance of 3.05 m from the interaction point (IP) along the z-axis (beam line).

6.1   Mechanical design

A possible mechanical design of the LumiCal is shown in Fig. 4. The calorimeter consists of two half barrels to allow for mounting on the beam pipe. Different bolt arrays carry the tungsten half disks and the sensor half layers. The two frames are decoupled, hence the silicon structure does not suffer gravitational sag due to the heavy, 600 kg, tungsten disks. The silicon sensors are glued on a 1 mm thick ceramic support. Some space is left for bonding.

The frame for the silicon layer has to fulfill the extreme precision requirements for the sensor positioning. In order to be able to survey the precision layers in the center of the device after mounting, the support ring contains holes. The precision of the optical survey must be in the μm range. The positions of the two half-barrels with respect to each other
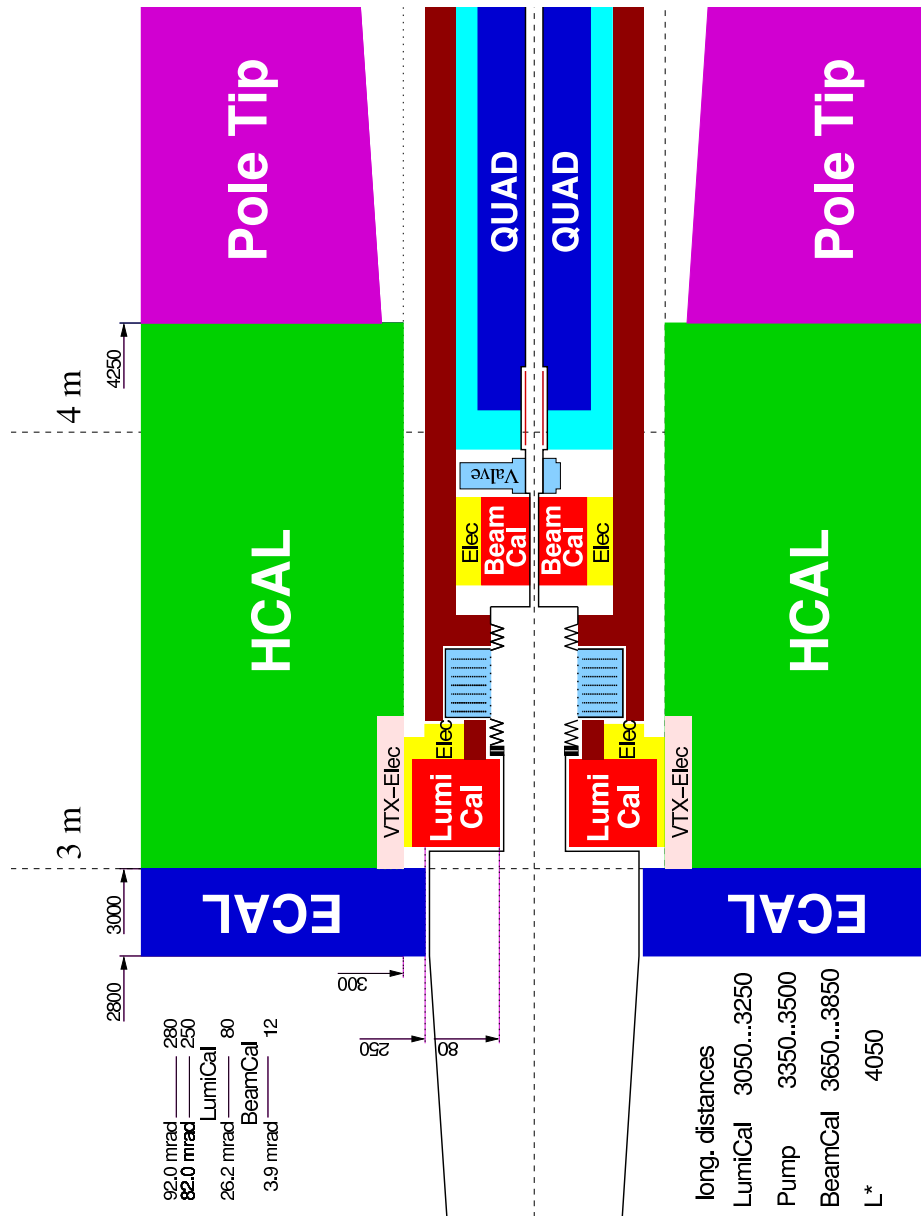
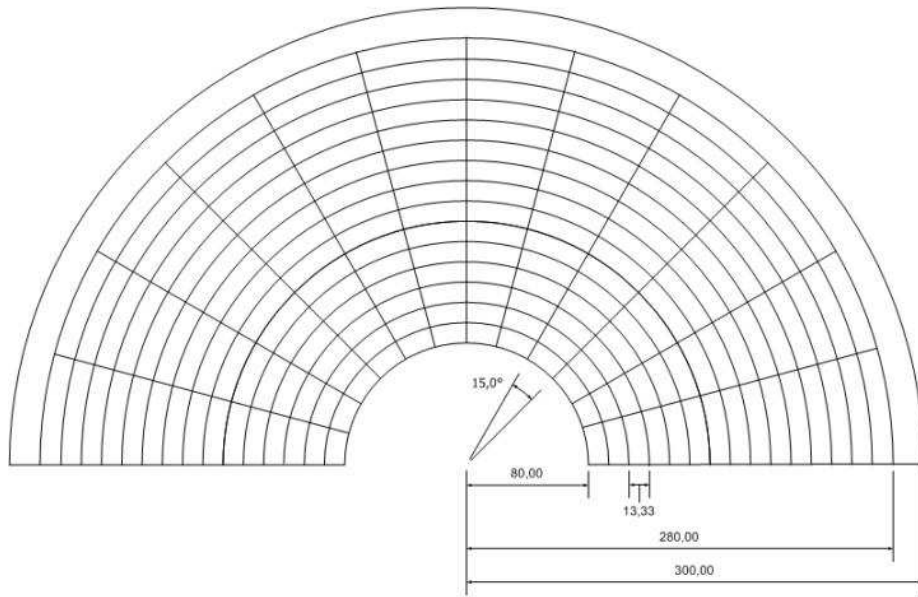Figure 2: Layout of the forward region [15].

Figure 3: Transverse subdividion of half a module, 15 cylinders and 12 sectors, is shown.

will be fixed through precise pins mounted at the top and bottom of each C shaped steel frame. The latter stabilizes the whole structure.

6.2 Alignment and Position Monitoring

The luminosity measurement requires precise alignment of the two LumiCal detectors with respect to each other and precise positioning with respect to the beam-line and the interaction point. The beam pipe is assumed to be a suitable reference. Also the beam position monitors are mounted at fixed positions inside the vacuum pipe. This would allow determining the actual LumiCal position with respect to the beam position.

The inner radius of the precision sensor layers must be known to 1 μm level, the accuracy in the transversal (x, y) displacement with respect to the beam is required to be known to 100 μm accuracy, and the distance between the two calorimeters along the beam axis must be known to an accuracy of 60 μm [18].

The position monitoring should not interfere with the mechanical support of the detector; hence an optical system is preferred. To measure the transversal displacement of the LumiCal detector with respect to the beam pipe, a laser system with a CCD matrix sensor is planned [14]. The radiation dose in this area will be probably sufficiently low.

The CCD sensor will be placed between the rear side of the LumiCal calorimeter and the tungsten shield. The radiation dose in that area will probably not be extremely high. The use of twin lasers in a parallel configuration is considered. The detector size easily
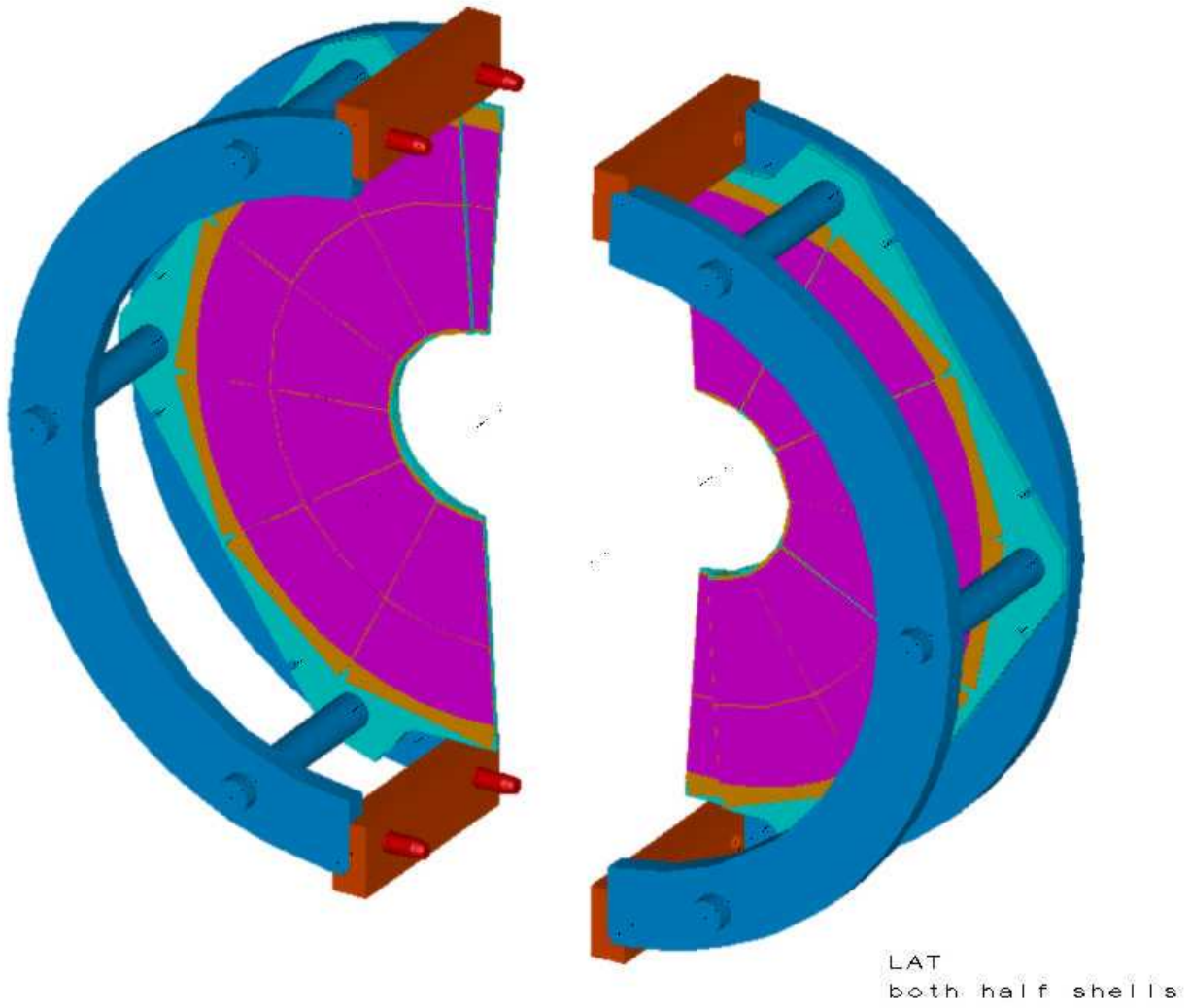
Figure 4: The LumiCal mechanical design [17].

allows for that and the algorithms can cope with two laser spots. Such a configuration assures better reliability in case of a laser failure.

6.3 Silicon Sensors

The silicon sensor tiles will be glued to a thick ceramic film plate supporting 6 sectors of the half-barrel. Readout chips will be placed radially outside the detector. We assume a 0.5 mm gap between the tiles and the sectors. The silicon pad diodes will be the usual planar silicon sensors. Reference marks are foreseen on the detector surface for precision positioning.

6.4 Electronics

The LumiCal electronics, especially the preamplifiers, must be carefully designed taking into account performance to be obtained from the more detailed MC simulations, limited space for electronics in the very forward region and acceptable heat dissipation. The large amount of readout channels favors the integration of the preamplifiers with the detector.

Connection from each pad to the preamplifier can be made using a Kapton flexfoil, a second metal layer with traces on the silicon surface or metal traces on the ceramic support plate. To ensure minimal cross talk from signals in adjacent sensors, Kapton flexfoil or traces on ceramics are preferred. The 0.5 mm gap between tiles is wide enough for bonding the pads or strips to traces on the ceramic support plate. On a sensor half-plane, up to 264 channels of the readout electronics need to be placed, requiring highly integrated chips.

Technology options are radiation hard CMOS or bipolar preamplifiers. The proper technology will be worked out in close collaboration with other sub-detector groups to find a standard solution.

7 Simulation of LumiCal response

Simulations of the LumiCal performance were done under three different conditions, with increasing level of sophistication of the physics case. Accordingly, the following sample were generated:

- Single positrons and electrons with energies between 50 and 400 GeV, uniformly distributed over the detector area.

- Bhabha scattering events (electrons, positrons and photons) at up to $\sqrt{s} = 800\,\mathrm{GeV}$, including initial and final state radiation, called pure Bhabha scattering events, hitting both arms of the detector.

- Bhabha scattering events including effects of nominal beam-energy spread and beam-strahlung.

For each sample, the detector response was investigated in details.

7.1 Single particles

Response to single electrons and positrons events was generated using the GEANT 3.21 [19] detector simulation package. Samples were generated for particles of energies 50, 100, 150, 200, 250 and 400 GeV. A uniform distribution in the polar and azimuthal angles of the particles was assumed. The particles were generated with θ covering the range $0.026 < \theta < 0.090$ rad.

These samples were used to study the basic properties of the detector such as energy calibration, energy and angular resolutions as well as for optimizing the reconstruction algorithm.

7.2 Bhabha events

The BHWIDE event generator [20] was used to produce Bhabha scattering events. The advantage of BHWIDE over the BHLUMI [7] generator is that it contains the electro-weak contributions, which are important for the high energy e^+e^- interactions considered here. The two generators were found to produce similar energy distributions for the final state particles.

Samples of 1000 events with center-of-mass energies of up to 800 GeV were generated with BHWIDE and were later processed through the GEANT detector simulation. These samples were used to understand the properties of Bhabha scattering events at high energy.

The spectrum of the sum of the electron and the positron energies for $\sqrt{s} = 500\,\text{GeV}$ is shown in Fig. 5. As expected, the energy peaks at 500 GeV and a long radiative tail towards lower energies is observed.
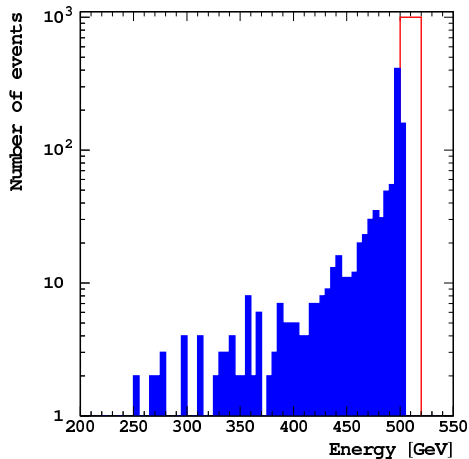

Figure 5: Distribution of the sum of the final state electron and positron fo Bhabha scattering events. The peak observed at 500 GeV corresponds to the intial energy.

The correlation between the e^- and the e^+ polar and azimuthal angles is shown in Fig. 6. For most of the events, the electron and positron are back to back. Events with different polar or azimuthal angles of e^- and e^+ are mostly due to initial state radiation.
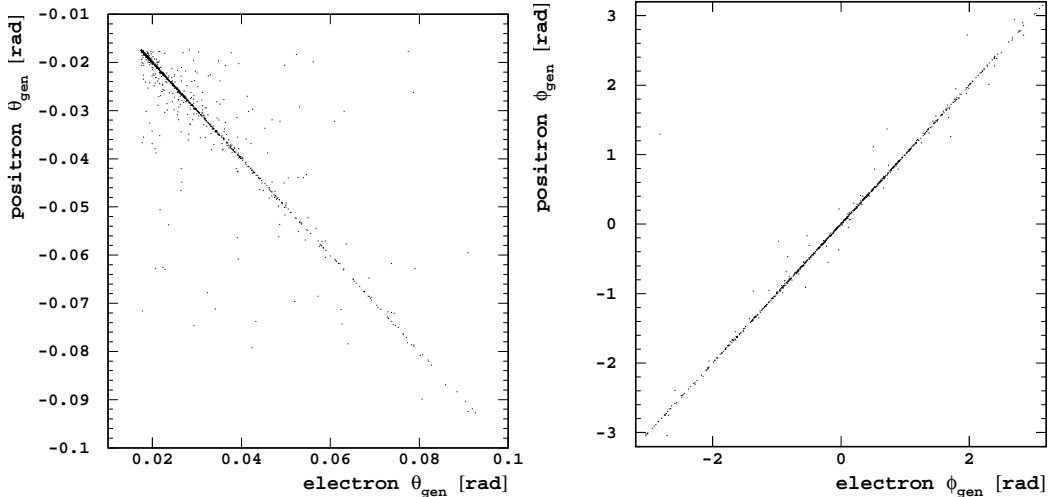
9

Figure 6: Correlation between the generated electron and positron scattering angle, θ_{gen} (left) and azimuthal angle ϕ_{gen} (right).

The multiplicity of photons generated by BHWIDE and their energy distribution are shown in Fig. 7. The average number of photons generated per event is 2.3. The majority of the photons have low energy and there is a long tail of photons with energies up to 240 GeV.

7.3 Beam spread

The center-of-mass energy in the collider will be known with an accuracy of 100 ppm. However, within a bunch the energy of the electrons and positrons is spread around the average value. To study this effect, a Gaussian beam spread was assumed and two cases were considered as input to BHWIDE,

- 0.05% spread from the center-of-mass energy, a number expected to be close to the actual beam-spread in the ILC (the number is estimated to be less than 0.1%),

- 0.5% spread from the center-of-mass energy, to assess a worst-case scenario.

7.4 Beamstrahlung

The CIRCE [21] generator was used to simulate the energy losses originating from beam-strahlung. These losses, together with the Bhabha scattering physics process per se, are the basis for understanding the energy spectrum of the collision.

The center-of-mass energy spectrum expected for a linear collider operated at a beam energy of 250 GeV is shown in Fig. 8. For completeness a spectrum with and without intial state radiation is shown. As can be seen in the figure, only a small part of the spectrum spread is due to beamstrahlung and beam-spread.
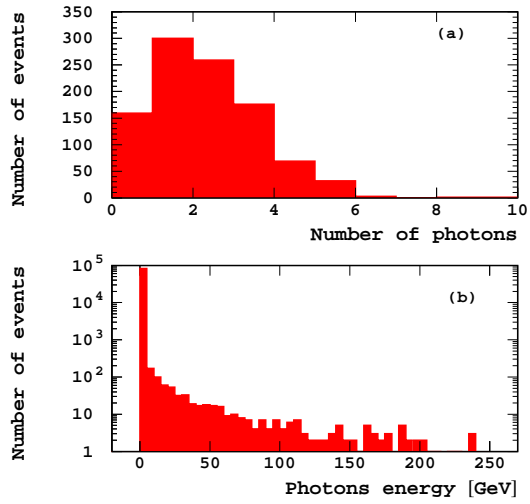
10

Figure 7: Distribution of (a) the number of photons and (b) of the energy of the photons obtained in BHWIDE.
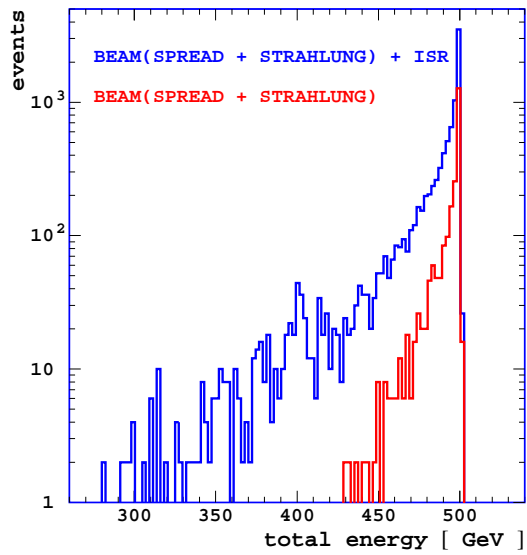

Figure 8: The energy spectrum including beam-spread and beamstrahlung, with (blue) and without (red) initial state radiation.

Most of the beamstrahlung radiation disappears down the beam pipe and does not hit the luminosity detector. A study of the background, originating from beamstrahlung and hitting the detector requires using an additional physics generator (GUINEA-PIG) and is beyond the scope of this study.

8 Detector Simulation

The luminosity detector simulation was performed using the BRAHMS [22] package based on the standard GEANT 3.21 [19] package for detector simulation.

The LumiCal geometry and definition of materials, was introduced into GEANT by the FCAL collaboration [23] as a common tool. Most of the studies of the detector performance were based on this implementation. In the optimization process, the LumiCal geometry in GEANT was modified accordingly.

9 Event selection

One of the key issues in the study of the LumiCal performance is the selection of Bhabha scattering events, which would minimize the systematic error derived from geometrical considerations and the background contribution.

The typical signature of Bhabha scattering events is the exclusive presence of an electron and positron, back to back in the detector. Because of the strong rise of the Bhabha scattering cross section towards lower polar angles, the lower angle acceptance is the most important parameter to control.

9.1 Fiducial volume (acceptance)

An algorithm was investigated in which only a few sensor-layers would govern the selection mechanism of contained electromagnetic showers. The cylinder structure of the detector offers a natural granularity in the θ angle.

The energy deposited in three layers located in the middle of the detector, close to the shower maximum, is divided into energy deposited in the edge cylinders, E_{out} and more centrally in the detector, E_{in}, as shown in Fig. 9.

The variable p, defined as

$$p = \frac{E_{out} - E_{in}}{E_{out} + E_{in}} \tag{3}$$

is then used to estimate the shower containment. Events with $p>0$ are rejected as being out of the acceptance region, while events with $p<0$ are kept. The behavior of the variable p as a function of the generated polar angle of the showering electron is shown in Fig. 10 for three different definitions of E_{out}, summed over one, two, or three cylinders. A given acceptance cut in θ can be translated into an appropriate number of edge cylinders. For a E_{out} summed over two cylinders, $p > 0$ corresponds to a θ cut of 33 mrad. The advantage of this method is its simplicity and the ability to define 'in' or 'out' without the full reconstruction process. The events were preselected using p calculated only for the electron detector arm.
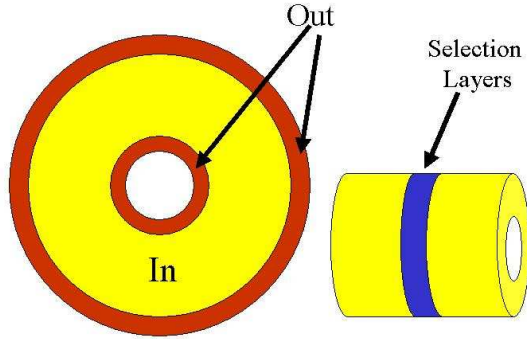
Figure 9: An illustration of the cylinders used in the calculation of the energy deposited outside, E_{out}, and inside, E_{in}, the acceptance region. The precision layers, situated where most of the energy is deposited, are marked in blue.
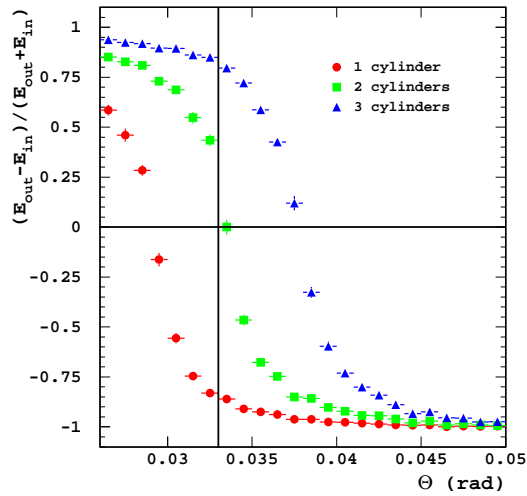

Figure 10: The variable $(E_{out}\text{-}E_{in})/(E_{out}+E_{in})$ as a function of the generated polar angle, θ, of the showering electrons for E_{out} summed over one (dots), two (squares) or three (triangles) inner cylinders.

9.2 Acolinearity selection

For head on collisions, the energy deposited in both arms of the detector will be similar and the showers of the electron and positron including final state radiation will be spatially back-to-back. At the generator level, most of the electrons and positrons originating from Bhabha scattering are indeed back-to-back in θ and in ϕ, as shown in Fig. 11. The Bhabha
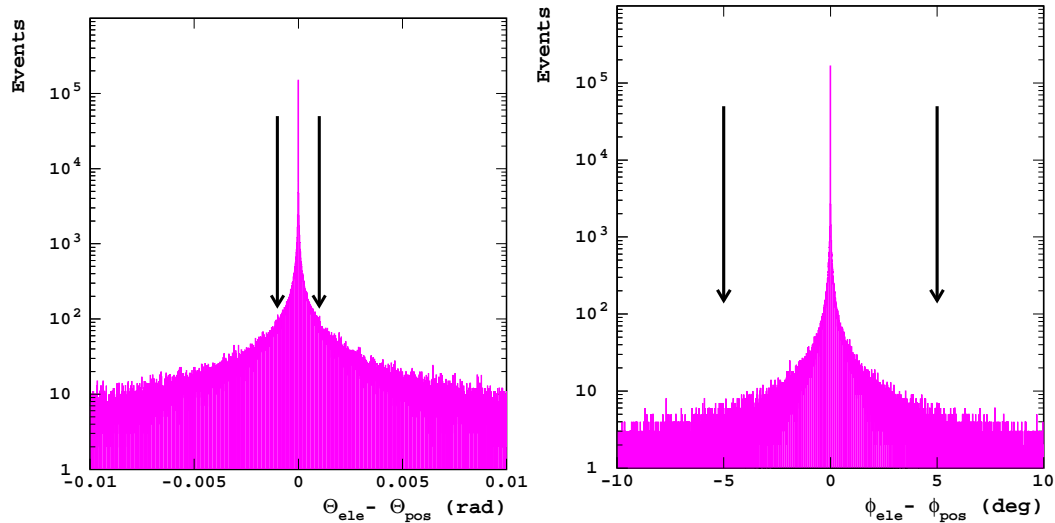
Figure 11: Left: distribution of the difference between the polar angles of the electron and the positron, $\theta_{ele} - \theta_{pos}$ at the generator level. Right: same for the azimuthal angle ϕ. The arrows mark the back-to-back acceptance region.

candidate events are selected by requiring the difference in the θ and ϕ angles be smaller than 20 times the respective reconstruction resolution (shown schematically in the figure).

In addition, the energy deposits on both sides of the detector are compared. The correlation between the signals deposited in the forward and backward arms of LumiCal are shown in Fig. 12 for a sample of Bhabha scattering events. In most of the events, the deposits on both sides are similar. The requirement of having back to back showers, with the electron shower contained in the fiducial volume, leaves the sample with events having almost the same energy deposits in the detectors. This is also shown in Fig. 13, where the energy deposits are shown as function of θ, before and after the selection.

10   Energy reconstruction and resolution

The energy resolution was studied for different physics samples and for a range of beam energies.
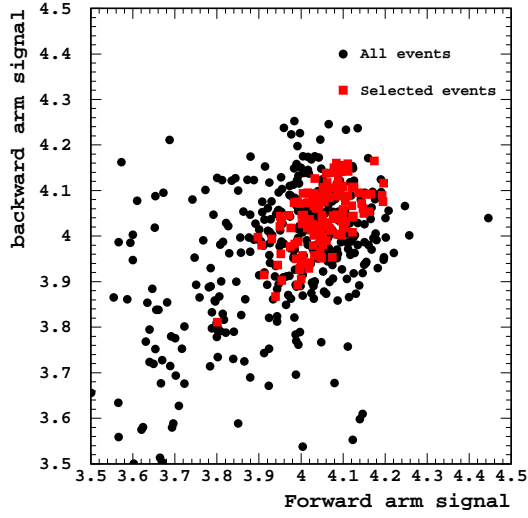
Figure 12: Correlation between energy deposited in the silicon sensors in the forward and backward arms of LumiCal for Bhabha events. The dark dots are for all events, and the lighter ones are for events for which the electron passes the fiducial cut and the two showers are back to back.
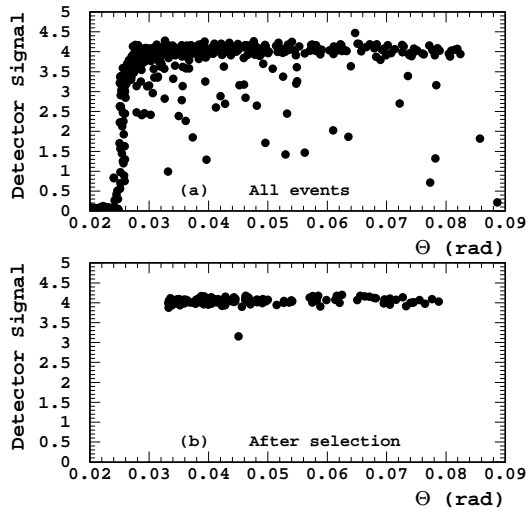

Figure 13: Correlation between the detector signal and θ angle, (a) for all generated Bhabha events and (b) only for the selected events.

10.1 Energy calibration

To get the signal of one event, the sum of the energy deposited in all the silicon cells is summed up for each event. No attempt to cluster the energy deposits was made. Assuming no leakage, the total deposited energy is proportional to the incoming energy of the absorbed particle. The response of the detector to single particles with different energies, ranging from 100 to 400 GeV, is shown in Fig. 14. As expected, with increasing beam energy the signal deposited in the silicon increases and the distribution becomes wider. The linearity
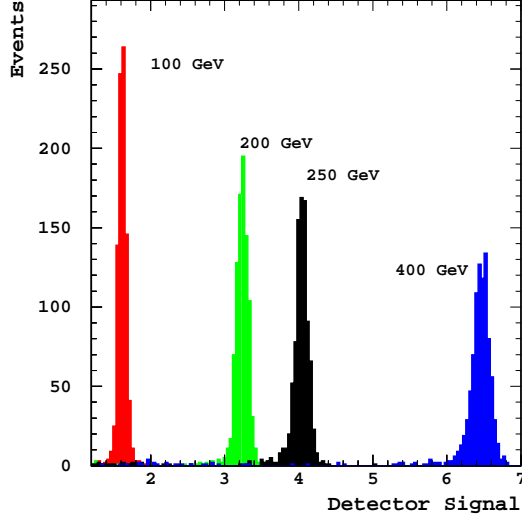
Figure 14: Detector response for single particles with four different beam energies, as denoted in the figure.

of the response is shown in Fig. 15, where the average deposit in the silicon is plotted against the energy of the absorbed particle. Only contained showers were used.

10.2 Detector resolution

The detector resolution is parameterized in terms of a, defined as

$$\frac{\Delta E}{E} = \frac{a}{\sqrt{E_{beam}}[\sqrt{G}eV]} ,$$ (4)

$\Delta E/E$ is determined from a Gaussian fit to every spectrum of deposited energy. The parameter a is then determined from a fit of formula (4) to the energy dependence of $\Delta E/E$.

Fig. 16 shows the energy resolution a as a function of the minimum θ angle of the showers, θ_{min}. The best resolution is achieved for θ_{min} of 33 mrad. Events entering the detector at a smaller angle are not fully contained.
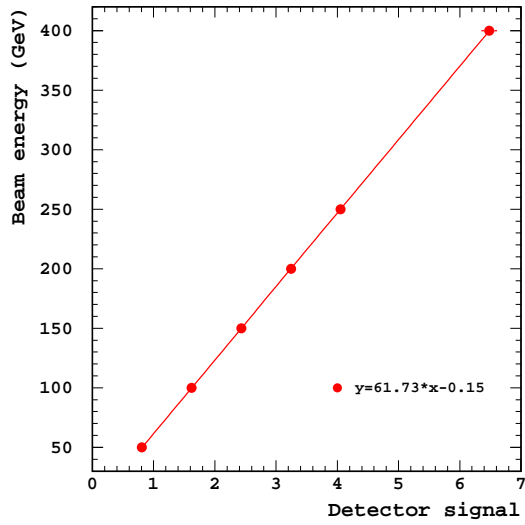
Figure 15: The beam energy as a function of the detector signal. The line is the result of a linear fit to the data points.
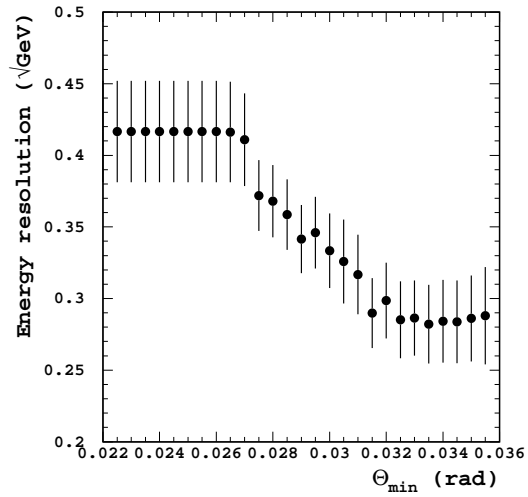

Figure 16: Energy resolution as a function of the minimum scattering angle used for acceptance, θ_{min}.

10.3   Results

The LumiCal response was studied as a function of energy for the various physics samples considered: single particles, Bhabha scattering, with and without beamstrahlung, with and without extra beam spread. The energy dependence of $\Delta E/E$ for selected events is shown in Fig. 17. The corresponding values for a are summarized in Table 1. The influence of
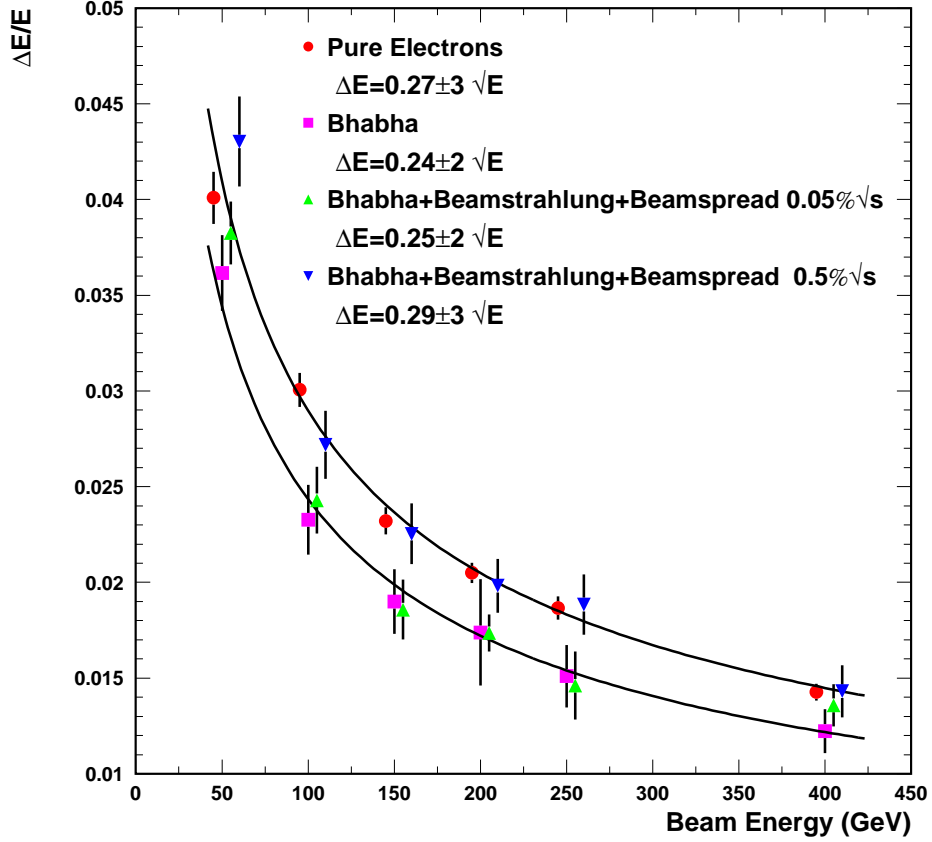

Figure 17: $\Delta E/E$ as a function of the beam energy, for four different physics samples, as denoted in the figure.

including non-contained events is also listed. In the most realistic physics case of Bhabha scattering with beamstrahlung and a beam spread of 0.05%, $a = (25 \pm 2)\%$.

The energy resolution for the case of single electrons/positrons appears to be slightly worse than for Bhabha events. The simulation of single electrons does not include final state radiation, as is the case for Bhabha events, and the total deposited energy is slightly lower compared to the Bhabha events.

The physics sample, with the extreme scenario of 0.5% beam-spread, results in a wider signal distribution and thus has the worst energy resolution. Without rejecting non-contained events, the resolution is by 30% larger.

Test sample	No cuts (%)	With cuts (%)
single electrons	31	27 ± 3
Bhabha events	42	24 ± 2
Bhabha + Beamstrahlung	45	24 ± 2
Bhabha + Beamstrahlung + Beam spread (0.05)	46	25 ± 2
Bhabha + Beamstrahlung + Beam spread (0.5)	49	29 ± 3

Table 1: Energy resolution a for different physics cases, before and after applying event selection cuts.

11 Polar angle reconstruction

In order to determine the polar angle of the particle impacting the calorimeter, a weighted average was introduced, where the weights are function of the energy deposition in the cells over which the angle is averaged,

$$< \theta > = \frac{\Sigma_i \theta_i W_i}{\Sigma_i W_i} \, . \tag{5}$$

One straight-forward method takes the energy deposited in a cell, E_i, as the weight

$$W_i = E_i \, . \tag{6}$$

This method is known to generate steps in the reconstructed values as a function of the generated one. A better approach is to use weights which are proportional to the logarithm of the energy deposits and to introduce a threshold on the deposits used for weighting [24],

$$W_i = \max\{0, [const + \ln \frac{E_i}{E_{tot}}]\}. \tag{7}$$

Here E_i denotes the energy deposited in cell i and E_{tot} is the total signal energy deposited in the calorimeter. The value of *const* is optimized to give the best possible resolution. This is depicted in Fig. 18, where the angular resolution σ_θ and the bias $\Delta\theta$ between the reconstructed and generated angles is plotted as a function of *const*. The value of *const* which minimizes the resolution also minimizes the bias. The improvement achieved over the linear weighting can be appreciated in Fig. 19, where the difference between the reconstructed and generated polar angles, $\theta_{rec} - \theta_{gen}$, is plotted against θ_{gen} for the two weighting options. The amplitude of the steps is drastically reduced (factor of three) and the general tilt (bias) is diminished. The optimization of the constant in the logarithmic weighting needs to be repeated for different beam energies. This can be seen in Fig. 20 where the dependence of σ_θ on *const* is plotted for three different energies. The value of *const* tends to increase with energy, as the energy deposited per cell increases.

In the design of LumiCal, the cell size increases with the distance from the beam line. As a result, the number of cells and sectors containing the shower decreases with θ (see Fig. 21). The number of cylinders being hit is affected by the leakage at the edge of the detector, so
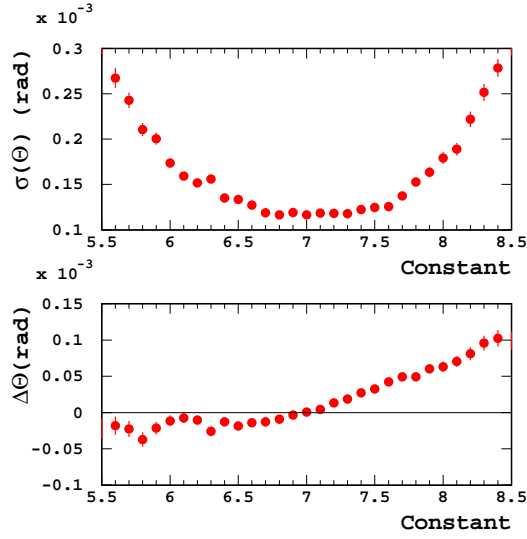
Figure 18: The polar angle resolution, $\sigma(\theta)$, and the polar angle bias, $\Delta\theta$, as a function of the threshold constant of the logarithmic weighting.
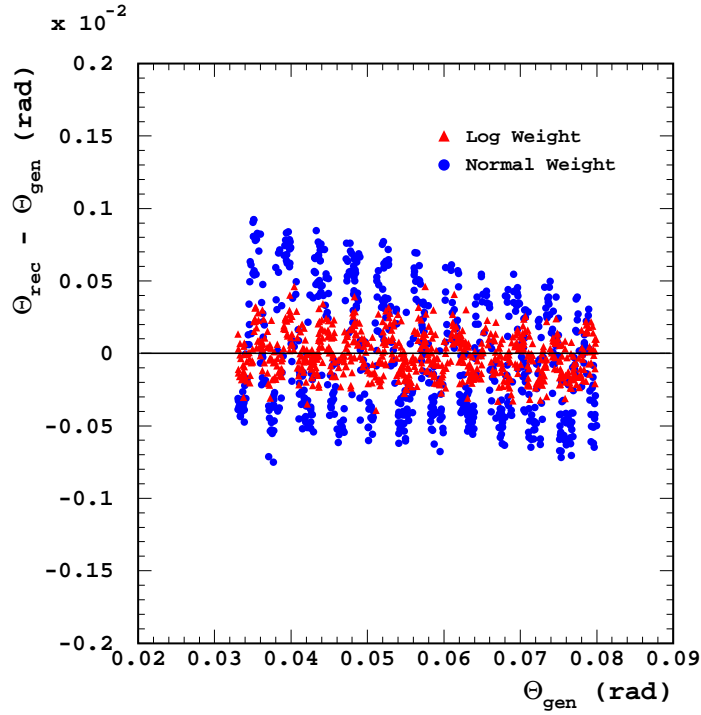

Figure 19: $\theta_{rec} - \theta_{gen}$ as a function of θ_{gen} for linear weights (dots) and for logarithmic weights (triangles).
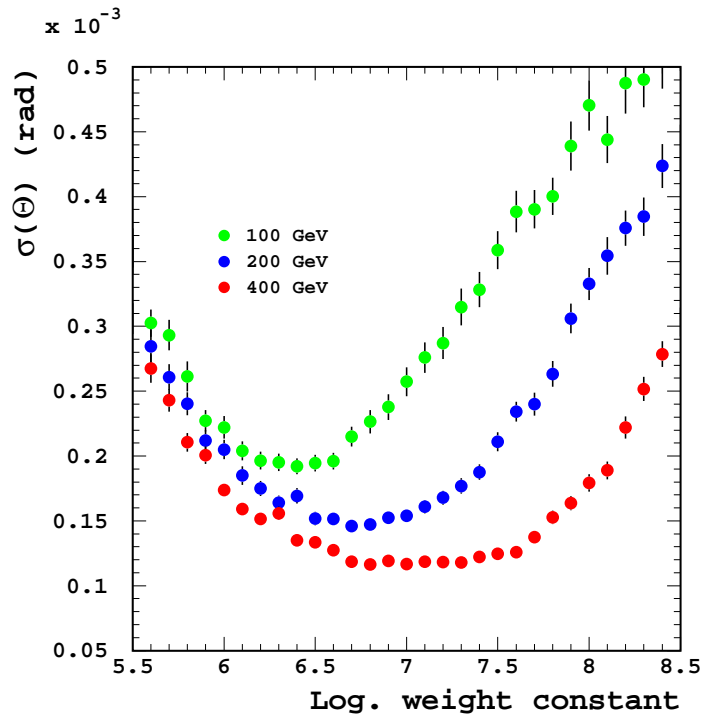
Figure 20: The polar angle resolution, $\sigma(\theta)$, as a function of the threshold constant in the logarithmic weighting, for three beam energies, as denoted in the figure.

that the highest number of hit cylinders is in the center of the detector. The logarithmic weighting eliminates this dependence and the number of cells, cylinders, sectors and rings contributing to the event reconstruction is θ independent. It is interesting to note that while the number of cells used in the logarithmic weighting is drastically reduced compared to the linear weighting, more than 90% of the total deposited energy is used. The polar
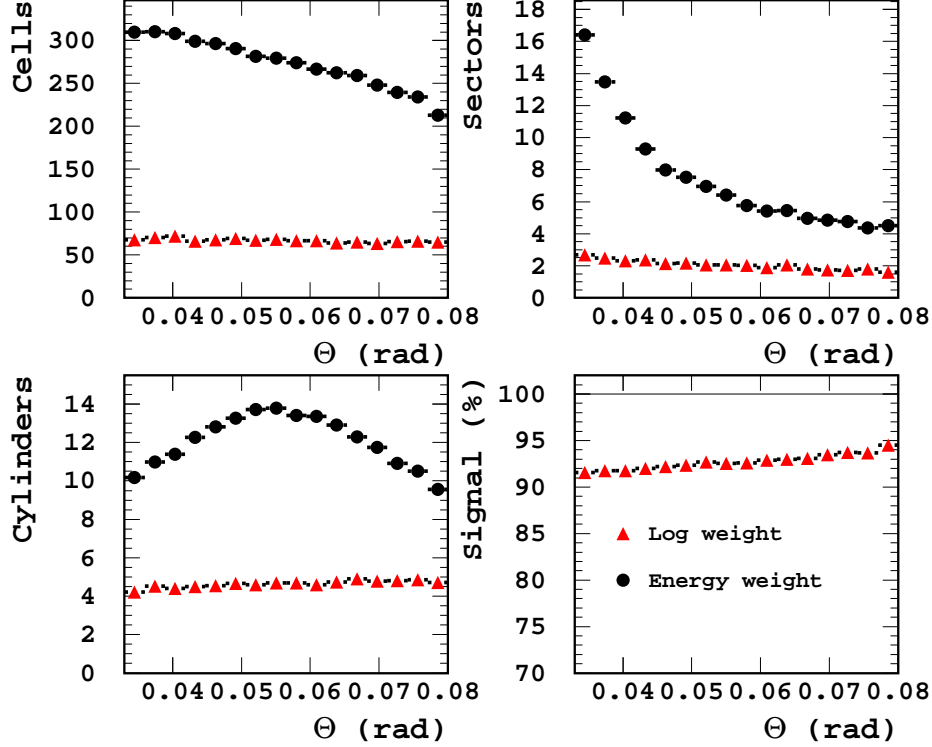

Figure 21: The average number of cells, sectors, cylinders and the percentage of the total deposited energy used in the linear and logarithmic weighting algorithms as a function of the scattering polar angle θ.

angle resolution improves with energy and is not sensitive to the type of simulated events. This is presented in Fig. 22.

In the nominal design of LumiCal, with 15 cylinders, the bias in the θ reconstruction is of the order of 10^{-4} (rad). This bias can be diminished by increasing the number of cylinders for the same θ coverage. The dependence of the bias of the number of cylinders is presented in Table 2 for 250 GeV electrons.

12   Reconstruction of the azimuthal angle

The logarithmic weighting algorithm is also used for ϕ reconstruction. Here also a dramatic improvement is observed. With a segmentation of 15° in ϕ, the resolution for 250 GeV

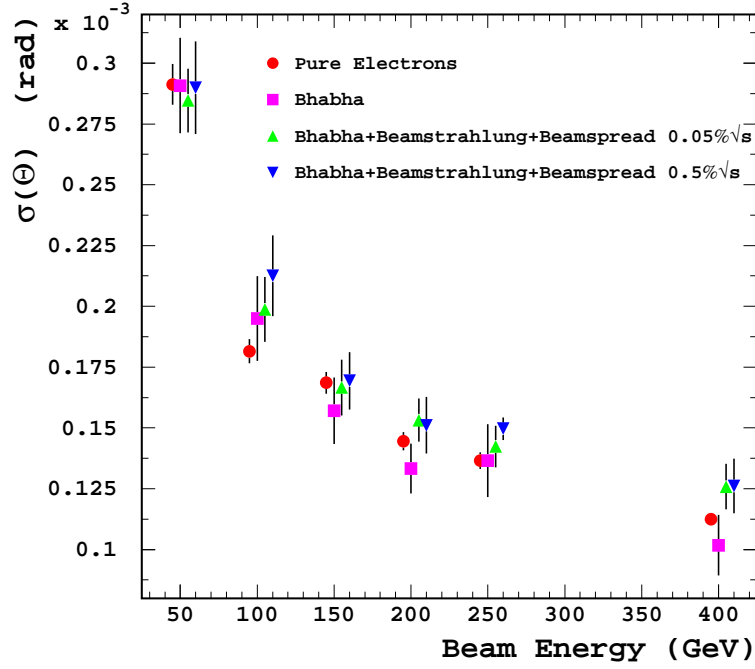Figure 22: The polar resolution, $\sigma(\theta)$, as a function of beam energy for different physics samples, as denoted in the figure.

Cylinders	Pitch in r (cm)	$\Delta\theta$ 10^{-5}(rad)
15	1.33	7
20	1.00	4
24	0.83	2
30	0.66	0.5

Table 2: The polar bias, $\Delta\theta$, as a function of the number of cylinders and their size.

electrons is found to be 0.63^o.

For the ϕ reconstruction, the θ dependence of the threshold in the logarithmic weighting is found to be significant. In Fig. 23, $\sigma_{(\phi)}$ is plotted as a function of the generated θ angle for three different weight functions. The linear energy weighting leads to a resolution of about 3°, almost independent of θ. The logarithmic weighting with a single value of *const* leads to σ_ϕ which changes as a function of θ and is in fact worse that for linear weighting, for low θ values. A $\sigma_\phi < 1^o$ and weakly dependence on θ can be achieved if *const* is optimized as a function of θ. The reason for this behavior is that in ϕ the cell size increases
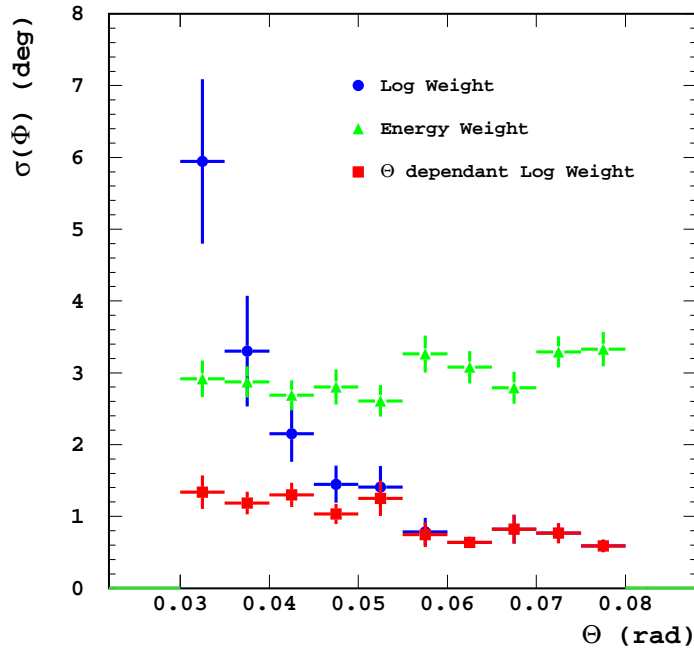

Figure 23: The azimuthal resolution, $\sigma(\phi)$, as a function of θ, for three weighting algorithms: linear energy weighting, logarithmic weighting and logarithmic weighting with a θ dependent constant.

with increasing θ. As a result, the number of cells and sectors being hit decreases with θ (see Fig. 24) and the energy deposited per cell increases, which leads to an increase in the threshold for optimal resolution. Note that the thresholds to be used in ϕ reconstruction are different from the ones for θ reconstruction and typically more than 98% of the deposited energy has to be used. It is interesting to note in Fig. 24 that for $\theta > 0.05$ rad, the same information is used in the linear and logarithmic weighting. Thus the improvement in resolution is solely due to the logarithmic weights.

The ϕ resolution as a function of the beam energy is shown in Fig. 25. As is the case for θ reconstruction, the resolution improves with increasing beam energy.
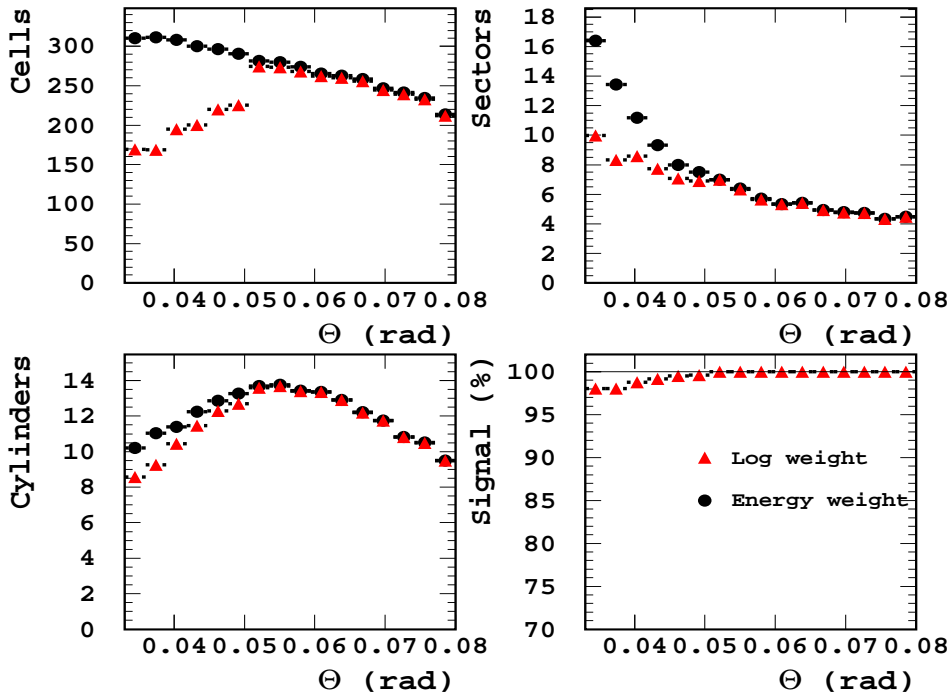
Figure 24: The number of cells, sectors, cylinders and the percentage of the signal used in reconstructing ϕ, as a function of θ, for the linear and logarithmic weighting algorithms, as denoted in the figure.
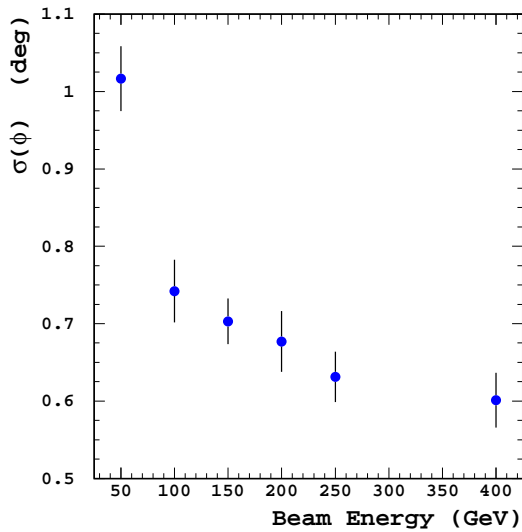

Figure 25: The azimuthal resolution $\sigma(\phi)$ as a function of the beam energy.

13 Performance Constraints

Until this point an ideal detector was assumed for the simulation. Hardware engineering and production design introduce constraints which may affect the detector performance. For some of these constraints, the impact on the detector performance can be evaluated by simulation.

13.1 Margins in between cells

The silicon sensors will be produced on a silicon wafer. Using available technologies, it is difficult to produce wafers to fit the LumiCal diameter. The current technology is based on a 6 to 8 inch wafer diameters. By the time of the LumiCal construction a 12 inch wafer would hopefully be available. It is thus more than likely that at the time of production few silicon wafers will have to be used and bond together. An example of how a 12 inch wafer could be used to build the sensors layer is presented in Fig. 26. In such a configuration,
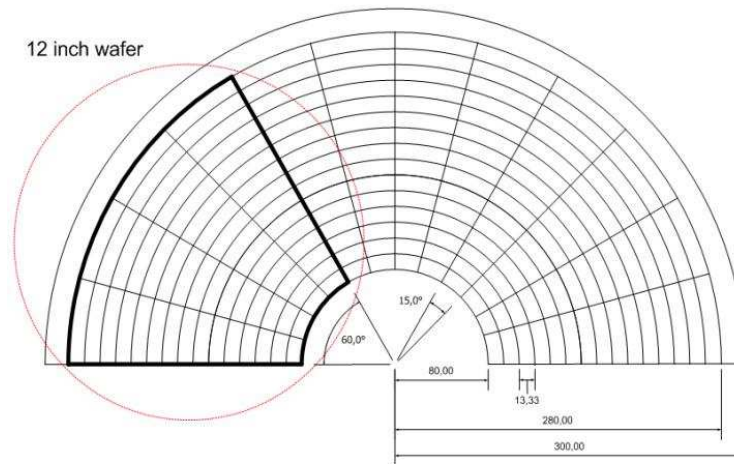

Figure 26: Upper half of a silicon layer in the LumiCal with a 12 inch silicon wafer overlayed.

margins along the wafer border area may be expected, creating an inactive area in the sensor plane.

A simple model is assumed, where every pad is surrounded by an inactive border and the inactive areas are aligned. The effect can be seen very clearly in the scan of the detector along the θ angle. A decrease in the signal can also be seen in the scan along the ϕ angle. This is shown in Fig. 27.

As can be seen in Fig. 28, with the increase of the inactive area the energy resolution and the angular resolution deteriorate. However for a margin size below a few microns, the deterioration is minimal. In the central region of the detector the energy resolution is better
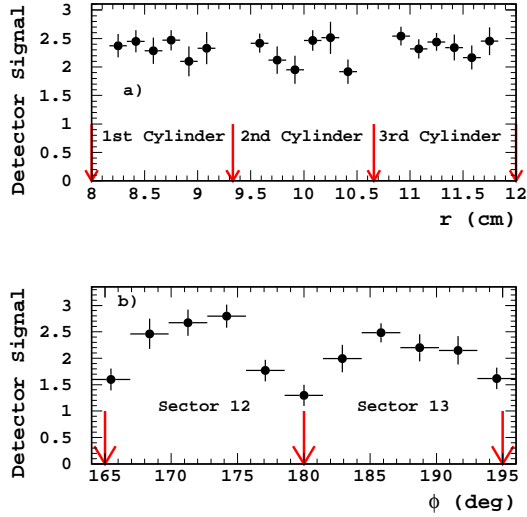
Figure 27: The detector signal as a function of (a) the position in radius and (b) in the azimuthal angle, ϕ. The results are for perpendicular impact of the particles and a case study of 2mm margins.

for small inactive areas while it gets worse for larger margins. Part of the problem may be avoided by reducing the overlap between pads in subsequent layers. This may be achieved by rotation of consecutive silicon layers by 7.5^o and by having two sets of cylinders, with different pitch.

13.2 Readout simulation

At this stage of the design studies there is no information about the noise level of the electronics. Therefore a simple model was considered where a Gaussian distribution centered around zero was assumed and the dependence of the response on its width was studied. In addition, the effect of possible dead cells was investigated.

13.3 Electronics noise

The addition of a Gaussian distributed noise results as expected in an increase of the energy resolution (parmeter a in Eq.4). The dependence of parameter a on the value of the noise to signal ratio is presented in Fig. 29. No marked change in the resolution is observed up to noise to signal ratio of 1/500. Above that, the resolution steadily deteriorates. A similar effect is observed for the angular resolution, as shown in Fig. 30. In the reconstruction of θ, an increase in the noise level results in the need to readjust the threshold for logarithmic weighting.

The noise to signal ratio for silicon sensors is expected to be of the order of 1/1000 and therefore the performance of the LumiCal should not be affected.
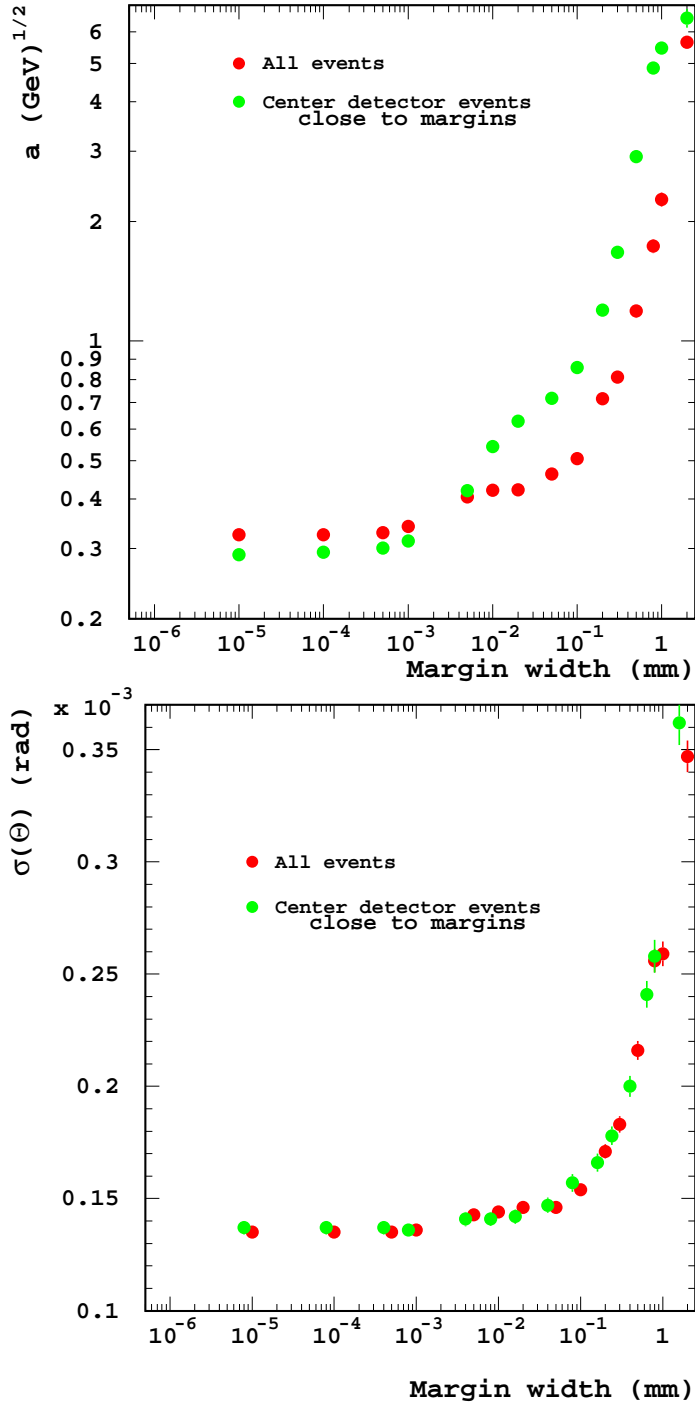
27

Figure 28: Above: detector energy resolution parameter, a ($\Delta E = a\sqrt{E}$) and below: the angular resolution, as a function of the size of the margin width, that is of the inactive area around each pad.
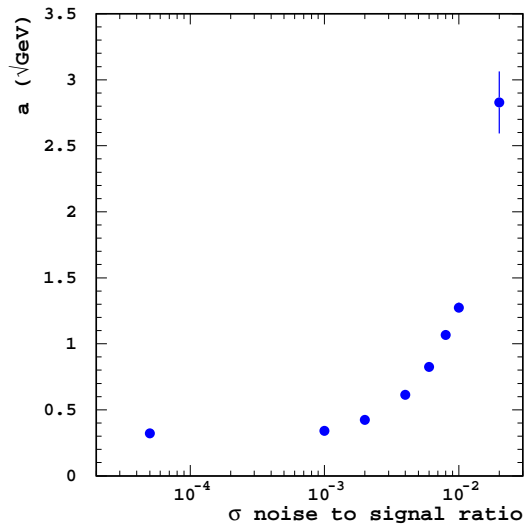
Figure 29: Energy resolution parameter, a ($\Delta E = a\sqrt{E}$), as a function of the noise width (σ noise) to signal ratio.
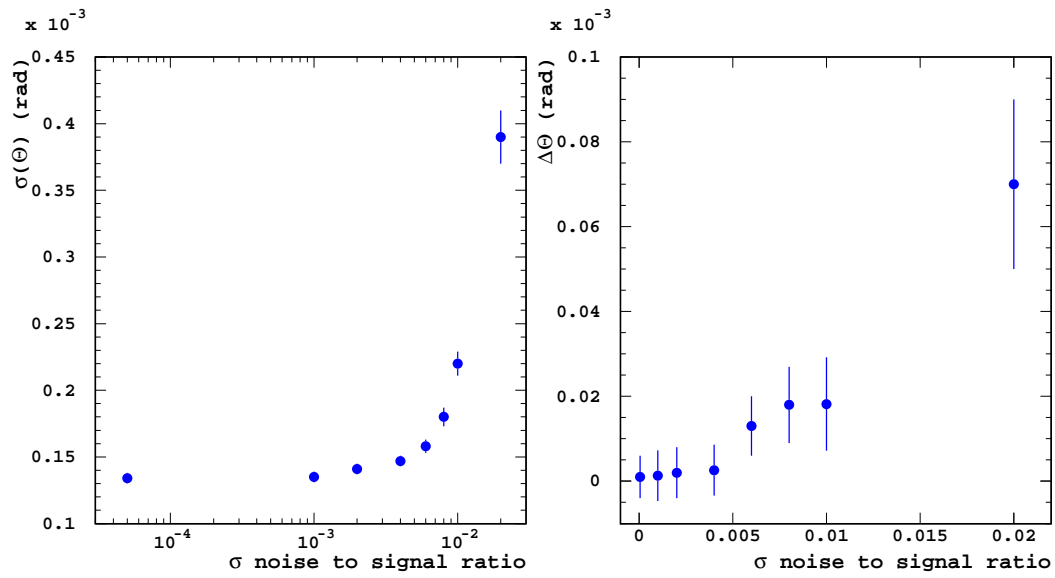

Figure 30: Left, the polar angle resolution, $\sigma(\theta)$ and right, the θ bias $\Delta\theta$ as a function of the noise width (σ noise) to signal ratio.

13.4 Dead cells

The LumiCal, a multi-channel detector, is very likely to have at some point dead channels. The tolerance to dead channels was studied by choosing randomly sets of dead cells with increasing size of the sets. Dead channels cause the detector signal to become smaller and the signal distribution becomes wider. The resolution deteriorates linearly with the increase of dead channels. This is shown in Fig. 31, where the energy resolution parameter is plotted against the percentage of dead channels. The percentage of dead cells used in
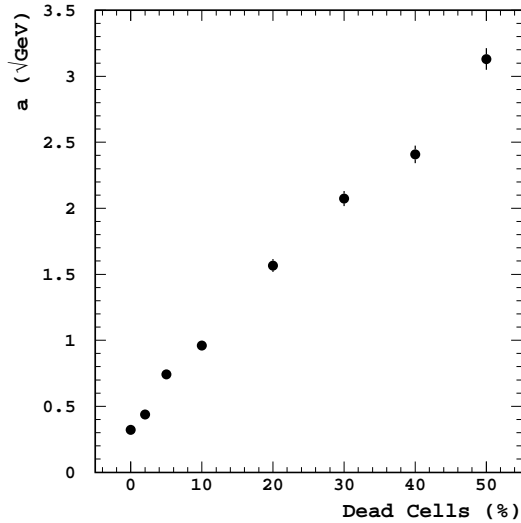

Figure 31:   The energy resolution parameter, a ($\Delta E = a\sqrt{E}$), as a function of the percentage of dead channels.

this study is for demonstration purposes only. A typical value expected after many years of running is at a few percent level. Some of the lost channels can be compensated for by using appropriate algorithms for filling in the lost information. This will result in a lesser effect on resolution.

14   Design Optimization

Various parameters of the LumiCal design were investigated in order to minimize the number of channels and maximize the performance. Subject to studies were length and segmentation.

14.1   Detector length

Originally the length of LumiCal was assumed to consist of 40 tungsten/silicon layers, each approximately one radiation length thick. In this configuration, the longitudinal shower profiles of single electrons were studied up to energies of 400 GeV.

The shower profiles and the corresponding integrands, for electrons of 50 to 400 GeV energy, are shown in Fig. 32. The energy deposited beyond 30 layers constitutes less than
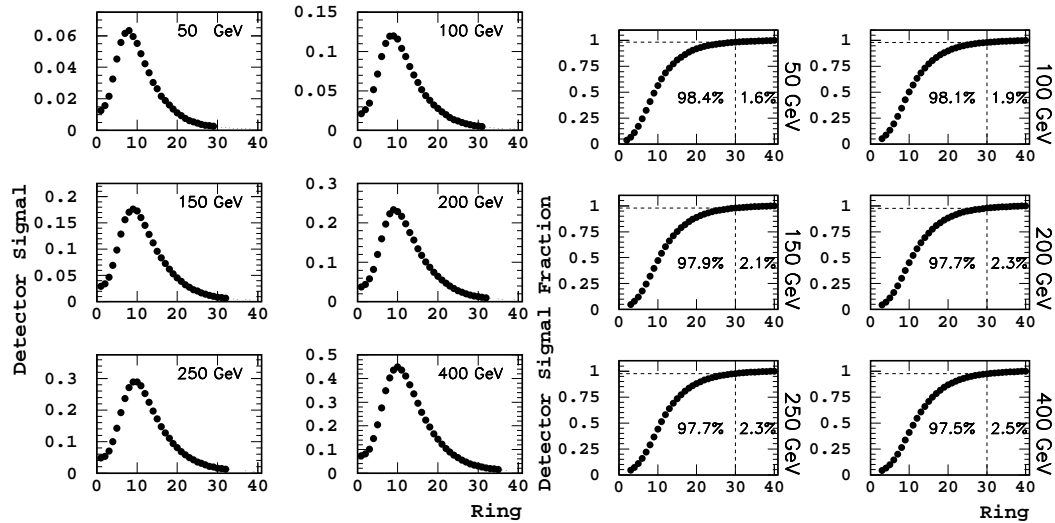

Figure 32: Left, longitudinal shower profile and right, the corresponding integrand as a function of depth, expressed in terms of detector rings, for showers generated for single electrons at different energies as denoted in the figure.

2.5% of the total deposited signal. Therefore, it was decided to limit the number of layers (rings) to 30, which leads to a LumiCal 20 cm long.

14.2 Segmentation

The quality and accuracy of θ angle reconstruction is the most important parameter in the systematics of luminosity measurement. The quality of θ measurement depends on the cell size, and the smaller the cell the better the performance.

The θ reconstruction is based on the logarithmic weighting and for each energy and cell size an optimal threshold has to be determined (see discussion in section 11). The dependence of the optimal threshold constant on the cell size is shown in Fig. 33. The threshold increases logarithmically with the cell size.

The dependence of σ_θ and $\Delta\theta$ on the number of cylinder subdivision, for 250 GeV electrons, is shown in Fig.34. The resolution obtained for 120 cylinders is an order of magnitude better than for 15 cylinders. Also the bias decreases steadily with decreasing cell size.

14.3 Shower peak design

In order to improve the polar resolution, a fine granularity is required. From the study of the logarithmic weighting algorithm it is clear that not all cells carry essential information.
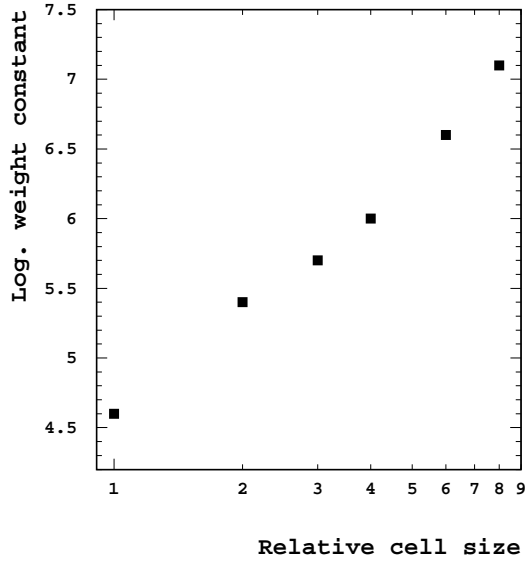
31

Figure 33: The threshold constant in logarithmic weighting as a function of the relative cell size, where one corresponds to a cell of a LumiCal subdivided into 120 cylinders.
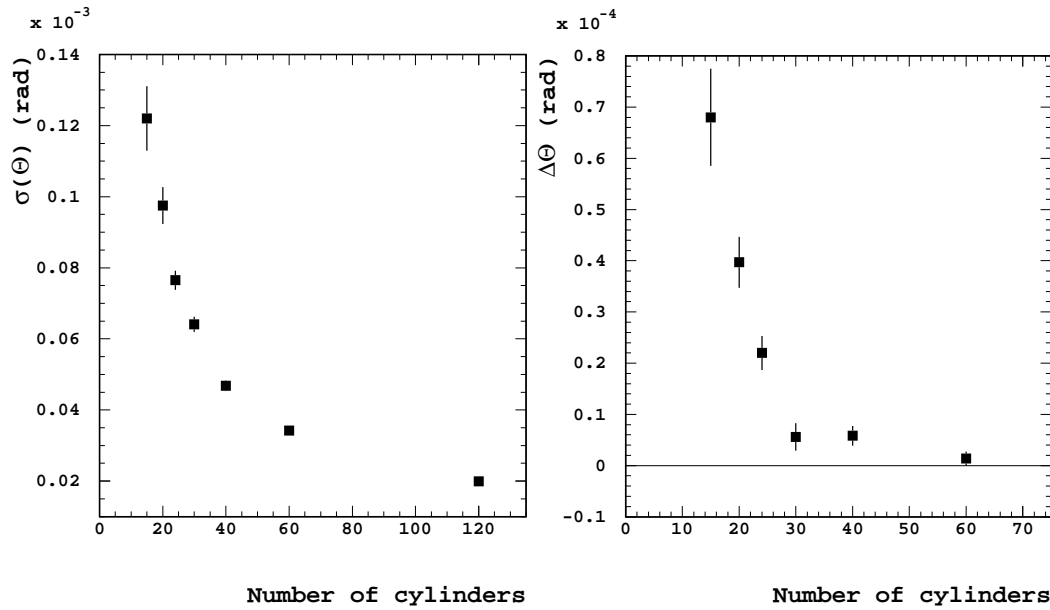

Figure 34: The polar angle resolution, $\sigma(\theta)$, and bias, $\Delta\theta$, as a function of radial subdivision expressed in terms of the number of cylinders.

One may therefore improve the position resolution by applying finer segmentation in the area of maximum energy deposits in the longitudinal development of the shower - in the area of the shower peak. In order to preserve the total number of channels, the segmentation of the remaining area may be decreased.

The following option was considered for the shower peak design: the front rings (1 to 4) and the back rings (20 to 30) were subdivided into 10 cylinders, while the middle rings (5 to 19) were subdivided into 20 cylinders. The longitudinal segmentation was not changed and the total number of channels (10800) was the same as for LumiCal subdivided into 15 rings throughout all the rings. The schematic representation of the shower peak design is shown in Fig. 35
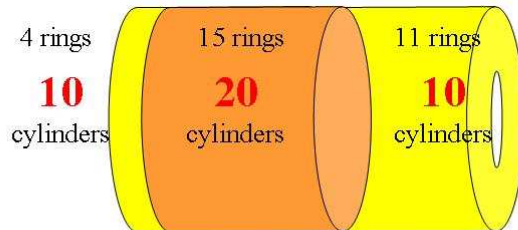

Figure 35: Schematic representation of the nominal design and the shower peak design of LumiCal.

The improvement in σ_θ can be seen in Fig. 36 where the θ resolution is plotted as a function of the threshold constant used in logarithmic weighting for the nominal design and the shower peak design. The best resolution is achieved for the same value of the threshold, however the shower peak design leads to a resolution of 11 mrad as opposed to 13 mrad in the nominal one. The θ bias, shown in the same figure remains unchanged.

The different utilization of the same number of cells results in improved detector per-
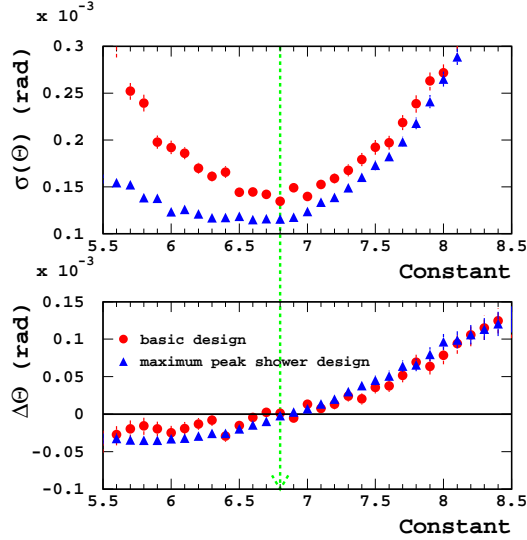
Figure 36: The polar resolution, $\sigma(\theta)$, and bias, $\Delta\theta$, as a function of the threshold constant used in logarithmic weighting for the nominal LumiCal design (dots) and the shower peak design (triangles).

formance. The disadvantage of the shower peak design is the need to design and build two sets of masks for two different cell sizes.

15 High Statistics Simulation

To achieve sensitivity to systematic effects comparable to the required relative precision on luminosity of 10^{-4}, large statistics MC samples are necessary. This cannot be achieved in a conventional manner, by processing events through a full GEANT simulation. Instead, a fast MC was developed, with smearing effects implemented through parameterization of the performance established on smaller samples. This MC allows detailed studies of various systematic effects, either related to geometry or possible mismatch between MC simulation and detector performance.

15.1 Analytic approximation

The θ dependence of the Bhabha differential cross section is given by

$$\frac{d\sigma}{d\theta} \sim \frac{1}{\theta^3},\tag{8}$$

and the total Bhabha cross section within a range of angles, θ_{min} and θ_{max} is then

$$\sigma \sim \frac{1}{2}(\theta_{min}^{-2} - \theta_{max}^{-2}) \sim \frac{1}{2}\theta_{min}^{-2},\tag{9}$$

34

where the θ_{max} dependence can be neglected. The relative error on the luminosity is then proportional to the relative error of the Bhabha cross section,

$$\frac{\Delta L}{L} = \frac{\Delta \sigma}{\sigma} \approx 2 \frac{\Delta \theta}{\theta_{min}} . \qquad (10)$$

The luminosity measurement is based on counting Bhabha scattering events in a well defined acceptance region. The error on the measurement is caused by miscounting events. The relative error on luminosity can then be written as

$$\frac{\Delta L}{L} = \frac{\Delta N}{N} = \frac{N_{rec} - N_{gen}}{N_{gen}} \bigg|_{\theta_{min}}^{\theta_{max}} , \qquad (11)$$

where N_{gen} and N_{rec} denote the number of events generated and reconstructed in the $[\theta_{min}, \theta_{max}]$ range.

15.2 θ reconstruction and luminosity

The influence of a bias in θ reconstruction on the luminosity error, obtained with fast MC simulation, is shown in Fig. 37. Sensitivity to shifts of the order of 10^{-4} are visible. The simulation reproduces well the expected analytical result of equation (10).
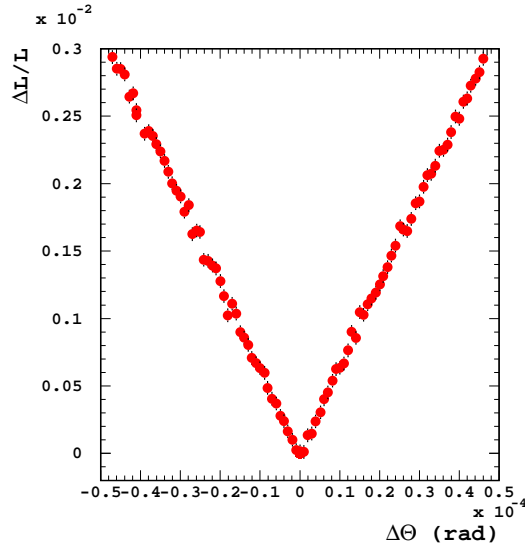

Figure 37: The relative error on luminosity, $\Delta L/L$, as a function of the θ bias, $\Delta \theta$, calculated using $5 \cdot 10^6$ Bhabha scattering events for each point.

To assess the effects of the θ resolution, the generated events were smeared with a Gaussian of width σ_θ centered at zero. The error on luminosity as a function of σ_θ, obtained just by counting events in a given generated and reconstructed θ range is shown in Fig. 38. For resolutions of the order of 0.1 mrad, as achieved in the simulated LumiCal, the error on luminosity is below the required precision even without correcting for effects of finite resolution.
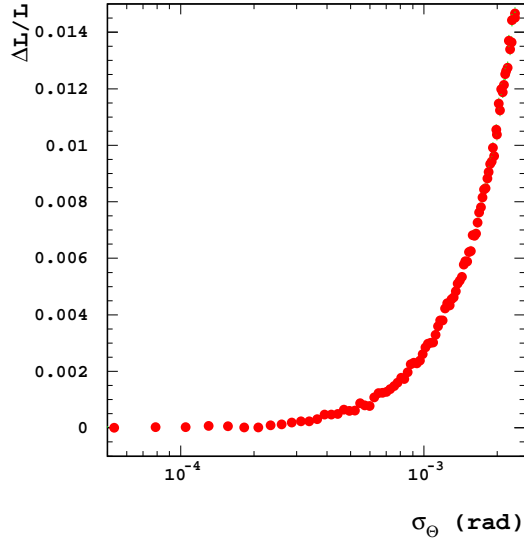
Figure 38: Expected relative error on luminosity due to finite polar angle resolution, as a function of this resolution σ_θ.

15.3   Positioning accuracy

Additional parameters affect the precision measurement of luminosity. Those pertaining to the positioning of LumiCal are listed in Table 3, together with the constraints imposed by the required precision on luminosity measurement. A full account can be found in [18].

16   Recommended design

The present study shows that to reach a precision $\Delta L/L = 10^{-4}$, a very good θ bias control is required. A pitch in θ of about 0.001 rad is needed. Segmenting the whole detector this way would lead to a very large number of electronic channels. The shower peak design study shows that the same performance can be obtained using half the electronic channels.

As a reminder, LumiCal is supposed to cover polar angles θ from 26 to 91 mrad with respect to the beam line. Longitudinally, the detector consists of layers composed of 0.34 cm of tungsten and 0.31 cm of electronics and silicon sensor (500 μm). To achieve the required bias in θ in the shower peak design, the segmentation would be as follows:

- the first 4 layers subdivided radially into 10 cylinders,
- the next 15 layers subdivided radially into 60 cylinders,
- the last 11 layers of the detector subdivided radially into 10 cylinders.

All layers are divided azimuthally into 24 sectors. Every other layer is rotated by 7.5 degrees in ϕ to minimize the margins effect. The cell transverse size is then 1/4 Moliére radius for the inner part and about 1.5 Moliére radius for the first four and the last 11 layers. The total number of electronic channels in one arm is 25,200.

$\Delta L/L$	$0.2 * 10^{-4}$	$1.0 * 10^{-4}$
inner radius	0.8 μm	4.2 μm
radial offset	290 μm	640 μm
distance of calorimeters	76 μm	300 μm
longitudinal offset	8 mm	18 mm
tilt of calorimeters	6 mrad	14 mrad
beam tilt	0.28 mrad	0.63 mrad
beam size	negligible	negligible

Table 3: Position requirements to achieve the required precision on luminosity measurement $\Delta L/L$. The numbers are taken from a dedicated LC note [18].

The performance of such a calorimeter is compared to that of the OPAL luminosity detector in Table 4. The latter did allow to determine luminosity with a relative error of $3.4 * 10^{-4}$. The main differences between the proposed design and the OPAL detector are due to the fact that LumiCal is located further from the interaction point and has a larger angular coverage.

The expected performance of this shower peak design is summarized in Table 5. The design performance properties lead to a systematic error on the luminosity measurement which, in the ideal case is better than 10^{-4}.

17 Summary

This note presents a Monte Carlo study of the performance of a tungsten-silicon sandwich calorimeter to be used for precision luminosity measurements at the future International Linear Collider. The study is focused on the precision with which the polar angle can be determined as it is a major component of luminosity measurement through Bhabha scattering event rates. Starting from a design similar to that used by the OPAL Collaboration, based on pad readout, a new design is proposed in which the segmentation of the calorimeter is adjusted to best probe the electromagnetic shower. Under ideal conditions, the proposed design would lead to a relative precision on luminosity measurement better than the required 10^{-4}.

18 Acknowledgments

Parameter	Opal	LumiCal
Distance from the IP	± 2.5 m	± 3.05 m
Sampling layers	19	30
Cylinders	32	60 (middle layers), 10 (first and last layers)
Sectors	32	24
Pitch in r (mm)	2.5	3.3 (middle layers), 20 (first and last layers)
Pitch in θ (rad)	0.001	0.001 (middle layers), 0.006 (first and last layers)
Pitch in ϕ (deg)	11.25	15
Pitch in z	1 X_0 2 X_0 (last 4 layers)	1 X_0
r_{min} (mm)	62	80
r_{max} (mm)	142	280
θ_{min} (mrad)	25	26
θ_{max} (mrad)	57	91
$z_{max} - z_{min}$ (cm)	14	20
Electronics channels in one detector arm	19,456	25,200

Table 4: Comparison between the designs of the Opal luminosity monitor and the proposed LumiCal.

Parameter	Performance
Energy resolution	25%
θ resolution	3.5×10^{-5} rad
ϕ resolution	0.63^o
$\Delta\theta$	1.4×10^{-6}
$\Delta L/L$	$< 10^{-4}$

Table 5: Summary of the expected performance of the proposed LumiCal design.

References

[1] S. Jadach, Theoretical error of luminosity cross section at LEP, hep-ph/0306083.

[2] J. Fleischer, A. Lorca and T. Riemann, Automatized calculation of 2-fermion production with DIANA and aITALC, hep-ph/0409034.

[3] K. Moenig, Physics Needs for the Forward Region, Talk given at Zeuthen FCAL meeting, Aug 2004.

[4] F. Jegerlehner, The role of $\sigma(e^+e^- \to$ hadrons) in precision tests of the Standard Model, DESY 03-189, hep-ph/0312372v1

[5] The SiW Group, Precision Luminosity for Lineshape Measurements with the OPAL Silicon-Tungsten Luminometer, OPAL Technical Note TN-528, 9 Dec 1997.

[6] G. Abbiendi et al., Precision Luminosity for Z^0 Lineshape Measurements with a Silicon-Tungsten Calorimeter, Eur. Phys. J. **C14** (2000) 373.

[7] S. Jadach et al., Upgrade of the Monte Carlo program BHLUMI for Bhabha scattering at low angles to version 4.04, Comp. Phys. Comm. **102** (1997) 229.

[8] M. Martinez, Workshop on Linear Collider, St.Malo 2002, see http://www-dapnia.cea.fr/ecfadesysstmalo/Sessions/QCD&top.

[9] TESLA Technical Design Report, see http://tesla.desy.de/new_page/TDR_CD/start.html ,Mar 2001, DESY-2001, ECFA-2001-209.

[10] The forward calorimetry group, 'R&D for the ILC-Detector: Instrumentation of the Very Forward region' DESY PRC R&D 02/01, status report April 18, 2006.

[11] M. Caffo, E. Remiddi, Bhabha Scattering, CERN-Report 89-08 **1** (1989) 171.

[12] R. J. Noblle, NIM **A256** (1987) 427.

[13] P. Chen, in Frontiers of Particle Beams, Lecture Notes in Physics, **296** (1988).

[14] U. Druhakou, R. Ingbir, K. Kousnetzova, W. Lohmann, L. Suszycki and W. Wierba, R&D for the TESLA-Detector: Instrumentation of the very Forward Region, DESY PRC R&D 02/01, Oct 2004.

[15] K. Busser and A. Stahl, DetectoConcept for the Forward Regions, LC-DET-2004-034.

[16] R. Ingbir MSc thesis, see http://alzt.tau.ac.il/~ronen/msc/msc.html, Jan 2006.

[17] U. Harder, Mechanical design of lumical, 5th FCAL workshop, DESY Zeuthen, 26th-28th August 2004

[18] A. Stahl, Luminosity Measurement via Bhabha Scattering: Precision Requirements for the Luminosity Calorimeter, LC-DET-2005-004, Apr 2005.

[19] R. Brun, F. Bruyan, M. Maire A. C. McPherson and P. Zanarini, GEANT3, 1984.

[20] S. Jadach, W. Placzek and B. F. L. Ward, BHWIDE 1.00: O(alpha)YFS Exponentiated Monte Carlo for Bhabha scattering at Wide Angles for LEP/SLC and LEP2 Phys. Lett. **B390** (1997) 298.

[21] T. Ohl, CIRCE version 1.0: Beam spectra for simulating linear collider physics, hep-ph/9607454.

[22] T. Behnke, G. Blair, M. Elsing, K. Monig, V. Mor gunov and M. Pohl, BRAHMS-Version 305, A Monte Carlo for a Detector at 500/800 GeV Linear Collider, see http://www-zeuthen.desy.de/linear_collider

[23] H. Abramowicz et al., Instrumentation of the Very Forward Region of a Linear Collider Detector, IEEE Transactions of Nuclear Science, **51** (2004) 2983.

[24] T. C. Awes et al., A simple method of shower localization and identification in laterally segmented calorimeters, Nucl. Inst. Meth. **A311** (1992) 130.